

Revisiting the influence of Fe excess in the synthesis of BaFe_2S_3 M. L. Amigó¹, Q. Stahl,² A. Maljuk,¹ A. U. B. Wolter,¹ C. Hess,^{1,*} J. Geck,^{2,3} S. Wurmehl,¹ S. Seiro,¹ and B. Büchner^{1,2,3}¹Leibniz IFW Dresden, Helmholtzstr. 20, 01069 Dresden, Germany²Institut für Festkörper- und Materialphysik, Technische Universität Dresden, 01069 Dresden, Germany³Würzburg-Dresden Cluster of Excellence ct.qmat, Technische Universität Dresden, 01062 Dresden, Germany

(Received 19 January 2021; revised 22 July 2021; accepted 19 August 2021; published 10 September 2021)

BaFe_2S_3 is a quasi-one-dimensional antiferromagnetic insulator that becomes superconducting under hydrostatic pressure. The magnetic ordering temperature T_N , as well as the presence of superconductivity have been found to be sample dependent. It has been argued that the Fe content may play a decisive role, with the use of 5 mol% ($\delta = 0.1$) excess Fe being reportedly required during the synthesis to optimize the magnetic ordering temperature and the superconducting properties. However, it is yet unclear whether a Fe off-stoichiometry is actually present in the samples, and how it affects the structural, magnetic, and transport properties. Here, we present a systematic study of compositional, structural, and physical properties of $\text{BaFe}_{2+\delta}\text{S}_3$ as a function of the nominal Fe excess δ . As δ increases, we observe the presence of an increasing fraction of secondary phases but no systematic change in the average composition or crystal structure of the main phase. Magnetic susceptibility curves are influenced by the presence of magnetic secondary phases. While a small excess Fe (2.5 mol%, i.e., $\delta = 0.05$) can slightly increase T_N and decrease the temperature of the resistivity anomaly at T^* , a range of T'_N/T^* 's is observed within each batch. This result strongly contrasts with the previously reported maximum of T_N at $\delta = 0.1$. Rather than with the value of δ , T_N and T^* seem to correlate with the broadening in the logarithmic derivative of the resistivity around T_N that could be an indicator of the level of disorder in the samples. Finally, we show that crystals free of ferromagnetic secondary phases can be obtained by remelting samples with nominal $\delta = 0.05$ in a Bridgman-like process based on optical heating.

DOI: [10.1103/PhysRevMaterials.5.094801](https://doi.org/10.1103/PhysRevMaterials.5.094801)

I. INTRODUCTION

In 2015, superconductivity under hydrostatic pressure was discovered in BaFe_2S_3 [1] and two years later in the related compound BaFe_2Se_3 under similar conditions [2]. Both chalcogenides present two salient differences to previously known iron-based superconductors. First, these materials are insulators and only become metallic and superconducting under pressure [1,3]. Second, $\text{BaFe}_2(\text{S}, \text{Se})_3$ does not present a two-dimensional layered crystalline structure, but rather a quasi-one-dimensional structure consisting of $\text{Fe}(\text{S}, \text{Se})_4$ tetrahedra forming two-leg ladders separated by Ba atoms [4]. The interest in materials having this geometry can be traced back to copper oxide structures. Dagotto and Rice proposed that quasi-one-dimensional cuprate quantum magnets already exhibit some of the key properties of the layered high- T_C cuprates, such as a spin gap, reminiscent of the pseudogap phase, or the emergence of superconductivity upon hole doping [5]. Two years later, these predictions were materialized in the cuprate $\text{Sr}_{14-x}\text{Ca}_x\text{Cu}_{24}\text{O}_{41}$ [6]. These qualitative aspects make the iron-based $\text{BaFe}_2(\text{S}, \text{Se})_3$ family a novel interesting platform to revisit the interplay between electronic correlations, effective dimensionality, and superconductivity [7–10].

At ambient pressure, BaFe_2S_3 shows a stripe-type antiferromagnetic order below $T_N \sim 120$ K [1,3,11]. As a function of hydrostatic pressure (P), T_N first increases and then presents an abrupt reduction at pressures near the insulator to metal transition ($P \sim 10$ GPa) [11,12]. In the metallic phase, superconductivity emerges, reaching a maximum critical temperature of ~ 24 K [1,3]. Both the presence of antiferromagnetic order and the emergence of superconductivity under applied pressure are similar to those of the parent compounds of the 122 (for example CaFe_2As_2 [13]) and 1111 (for example LaFeAsO [14]) iron pnictide families.

However, the reported properties of BaFe_2S_3 samples depend on the synthesis procedure [1,15]. In Ref. [1], samples grown using excess Fe were found to exhibit the largest T_N , as well as superconductivity under hydrostatic pressure, while samples grown from a stoichiometric ratio of precursors yielded a low T_N and no superconductivity up to 20 GPa. This suggested the presence of a slight Fe deficiency as a detrimental factor for both magnetic order and superconductivity. A systematic study as a function of the excess Fe used in the synthesis reported the maximal T_N , identified as a dip in the magnetic susceptibility, for samples grown using 5 mol% excess Fe. The samples grown starting from this composition were assumed to present the true 123 stoichiometry based on energy-dispersive x-ray spectroscopy and resistivity measurements [16].

The correlation of the actual Fe content in the crystals with the crystal structure and the characteristic temperatures is still

*Present address: Fakultät für Mathematik und Naturwissenschaften, Bergische Universität Wuppertal, 42097 Wuppertal, Germany.

unknown, mostly due to the paucity of systematic studies. It is yet unclear whether and to which extent the excess Fe used in the reaction is really incorporated into the crystal structure or only forms secondary phases and, in the last case, which is the effect of these extra phases in the measured physical properties like magnetization or resistivity. In this paper, we fill this gap presenting a comprehensive study of $\text{BaFe}_{2+\delta}\text{S}_3$ as a function of the nominal Fe excess δ used during growth. For this, we characterized in detail the composition and the crystal structure as well as the magnetization and the transport properties as a function of δ . We observe no clear correlation between the nominal δ and the actual composition and structure of BaFe_2S_3 crystals. A large spread of transition temperatures within a batch and an increasing amount of impurity phases were observed upon introducing excess Fe in the reaction. Ferromagnetic impurities could be suppressed by using a Bridgman procedure to grow crystals from a melt with a slight Fe excess. This article is organized as follows. In Sec. II, methodological aspects are presented. Section III shows the topography and the composition of our samples (III A), powder and single crystal x-ray diffraction (III B), magnetization (III C), and resistivity results (III D). Section IV presents the discussion of our results. Finally, Sec. V contains our conclusions.

II. METHODS

Single crystals were grown from powders of BaS (Alfa Aesar 99.7%), Fe (Acros organics 99%), and S (Alfa Aesar 99.5%) in the molar ratio $1 : 2 + \delta : 2$ with $\delta = 0, 0.05, 0.1, \text{ and } 0.2$. The powders were thoroughly mixed using an agate mortar inside a glovebox under an inert Ar atmosphere and placed in a carbon glass crucible. A quartz ampule containing the crucible was sealed under vacuum. We placed the quartz ampule in a vertical position inside a Nabertherm programmable chamber furnace and heated up to 1100°C . This temperature is above the reported melting point of BaFe_2S_3 [4] but below the melting point of BaS [17] and Fe [18]. Then, the temperature was lowered to 750°C at 3°C/h . From this slow decrease through the melting point of BaFe_2S_3 , we obtained an ingot at the bottom of the crucible from which needle-like single crystals of mm length could be mechanically detached.

For the case of $\delta = 0.05$, we also studied the effect of remelting the obtained samples using a Bridgman procedure in a floating-zone furnace. For this, the ingot obtained in the previous step was ground into a powder and put in a quartz ampule. The powder was melted by optical heating in a 4-mirror type image furnace produced by CSI (Japan) using 1 kW halogen lamps as a heat source. The completeness of powder melting was controlled by means of a CCD camera and direct visual (by protected eyes) observation. It is worth to mention that optical heating provides a steeper temperature gradient on the crystallization front compared to a conventional Bridgman method based on resistive heating, and a considerably steeper gradient than the “self-flux” like method generally used to grow BaFe_2S_3 . Prior to the growth, the furnace chamber was evacuated up to 0.01 mbar and purged with Ar (5N) gas 3 times in order to remove oxygen from the chamber atmosphere. The quartz container had an

inner diameter of 11 mm and wall thickness of about 1.5 mm. Quartz glass presents the advantage of an extremely high thermal shock resistance, good optical transmission in visible and near-IR ranges and is relatively chemically inert. The initial powder was melted at 73% of lamps power under 7.5 bars Ar pressure. Then the glass container with the melt was pulled down at 1.6 mm/h and it was rotated at 12 rpm. A solidified ingot of ~ 15 mm in length was mechanically detached from the cracked quartz container, from which single crystals could be easily broken off. Only slight traces of evaporation were observed on the inner wall of the quartz ampule.

In the rest of this article, we are going to identify the samples by the nominal Fe excess, δ , and use the label “remelted” for the samples grown using the Bridgman technique.

We studied the topography and the composition of the samples in a Zeiss EVOMA15 scanning electron microscope (SEM) with AzTec software equipped with an electron microprobe analyzer for semi-quantitative elemental analysis using the energy dispersive x-ray (EDX) mode. To improve comparability of results between samples, we used a common plane surface. For this, we embedded the samples together prior to polishing and performed measurements for all batches under the same conditions. This approach has been successfully used to distinguish composition trends well below the typical EDX accuracy in other compounds [19]. We used BaF_2 and FeS_2 as standards. The studied samples were for each batch a piece of crystals’ conglomerate with a size of $\sim 1 \times 2 \times 3 \text{ mm}^3$, containing several needle-like single crystals. We performed more than 50 measurements for each batch of samples, retaining only data sets where the total weight percent (wt%) was between 95 and 105 wt%. The measurements were distributed over the whole surface of the samples.

Powder x-ray diffraction experiments were carried out at room temperature on crushed single crystals in a STOE STADI P diffractometer equipped with a MYTHEN 2K detector using $\text{Mo-}K_{\alpha 1}$ radiation. The data were analyzed using the FullProf Suite program [20]. The March-Dollase multi-axial model for preferred orientation was used in the refinements.

Single-crystal x-ray diffraction data were collected at 295 K on a Bruker-AXS KAPPA APEX II CCD diffractometer with graphite-monochromated $\text{Mo-}K_{\alpha}$ x-ray radiation (50 kV, 30 mA). The crystal-to-detector distance was 45.1 mm and the detector was positioned at a 2Θ position of 30° for the measurements using an ω -scan mode strategy at four different ϕ positions ($0^\circ, 90^\circ, 180^\circ, \text{ and } 270^\circ$). All data processing was performed in the Bruker APEX3 software suite [21], the reflection intensities were integrated using SAINT [22] and multiscan absorption correction was applied using SADABS [23]. The subsequent weighted full matrix least-squares refinements on F^2 were done with SHELX-2012 [24] as implemented in the WinGx 2014.1 program suite [25]. The crystal structures were refined with anisotropic displacement parameters for all atoms. The used lattice constants were determined via Rietveld refinement of the corresponding powder patterns.

Magnetization measurements were carried out in a vibrating sample superconducting quantum interference device magnetometer (SQUID-VSM) from Quantum Design. The magnetic field was applied parallel to the needle direction. For all measurements, we used a zero-field cooling procedure

(ZFC). To reduce the value of the residual magnetic field, to less than 2 Oe, we applied a field of 5 T at room temperature and then removed it in an oscillation mode. This procedure was performed before each temperature or field dependence magnetization measurement.

For the resistivity measurements, we used a dip-stick setup immersed in a Dewar with liquid He. A standard four probe method was used. The electric contacts were made with silver paste and gold wires of a diameter $\sim 25 \mu\text{m}$. The current was applied along the needle direction.

III. RESULTS

A. Topography and composition characterization

Secondary electron (SE) and back-scattered electron (BSE) images for $\text{BaFe}_{2+\delta}\text{S}_3$ samples with nominal $\delta = 0$ are shown in Figs. 1(a) and 1(b). Owing to their quasi-one-dimensional structure, the samples are difficult to polish, as attested by the characteristic needle-like striations observed in scanning electron microscope images. While an increase from $\delta = 0$ to 0.2 would imply a theoretical increase of 2.15 at% in the Fe content, the composition averaged over large areas of the main phase (~ 50 measurements distributed in an area of $\sim 2 \times 3 \text{ mm}^2$ per batch) shows no monotonic change as a function of δ , as summarized in Table I. This contrasts the previous report of a monotonic increase in the Fe content up to $\delta = 0.1$ as a function of δ determined from 5 points on one single crystal for each δ [16]. Moreover, the average

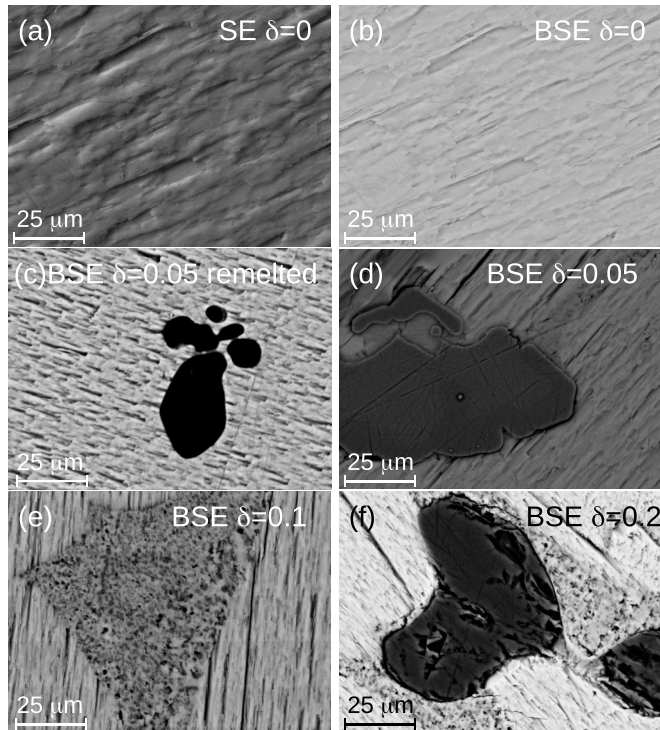


FIG. 1. (a) Secondary electron SEM image of $\text{BaFe}_{2+\delta}\text{S}_3$ for $\delta = 0$. Back-scattered electron SEM images for (b) $\delta = 0$ and for inclusions of (c) a Si-rich phase for $\delta = 0.05$ (remelted), (d) Fe for $\delta = 0.05$, (e) other ternary phases containing Ba, Fe, and S for $\delta = 0.1$, and (f) FeS for $\delta = 0.2$.

TABLE I. Average composition (at%) of the main phase as a function of the excess Fe in the nominal composition δ for $\text{BaFe}_{2+\delta}\text{S}_3$. The numbers in parenthesis correspond to the standard deviation. Expected (theoretical) values are also indicated for $\delta = 0$ and 0.2.

δ	Ba	Fe	S
0 (theoretical)	16.67	33.33	50.00
0	17.2(2)	32.9(2)	49.9(3)
0.05 (remelted)	16.9(2)	33.2(5)	49.9(4)
0.05	17.1(2)	32.8(2)	50.1(4)
0.1	16.8(2)	32.3(4)	50.9(5)
0.2	17.0(3)	32.9(4)	50.1(6)
0.2 (theoretical)	16.13	35.48	48.39

composition of the main phase for each batch is consistent with BaFe_2S_3 within the accuracy of the method [19,26]. Within a batch, the composition of each element measured over the main phase differs by less than 0.6 at%. The standard deviation of the compositional data slightly increases as δ increases suggesting a higher chemical inhomogeneity in the main phase. The measured standard deviation could however be influenced by the presence of secondary phases or voids beneath the surface.

Figures 1(c)–1(f) show typical inclusions found in the samples. FeS was observed in the crystals with a nominal Fe content of $\delta = 0.1$ and 0.2. Moreover, Fe was identified as an inclusion for crystals with $\delta = 0.05$ and 0.2. Other small-sized areas with varying amounts of Ba, Fe, and S were also observed. Some measurements presented a small quantity of O, which could have originated from residual oxygen present in the ampule during growth, or from oxidation of the inclusions during the preparation of the samples for the measurements. No presence of O was observed in the main phase. In the case of $\delta = 0.05$ (remelted) a small quantity of a Si-rich phase was found, which possibly indicates a reaction between the melt and the quartz crucible.

Our chemical analysis suggests that the Fe content in the main phase is practically unchanged and the excess Fe used during synthesis mostly leads to the formation of Fe rich secondary phases. The batch with $\delta = 0.1$ yielded a slightly (less than 1 at%) lower average Fe content than the others, but as will be shown below, the physical properties for this batch are not significantly different.

B. Structural characterization

1. Powder x-ray diffraction

Powder x-ray diffraction data for samples with different nominal Fe compositions are shown in Fig. 2(a). Most reflections can be identified with the orthorhombic structure with space group $Cmcm$ (No. 63) previously reported for BaFe_2S_3 [4]. The differences in the relative intensities of the reflections, in particular for $\delta = 0.05$ (remelted) and 0.1, are most probably related to a preferred orientation of the powder, given the highly anisotropic nature of the crystal structure and the needle-like morphology of the crystals. The lattice parameters were obtained from a Rietveld analysis and are listed in Table II. As an example of the refinement, the case of $\delta = 0.05$

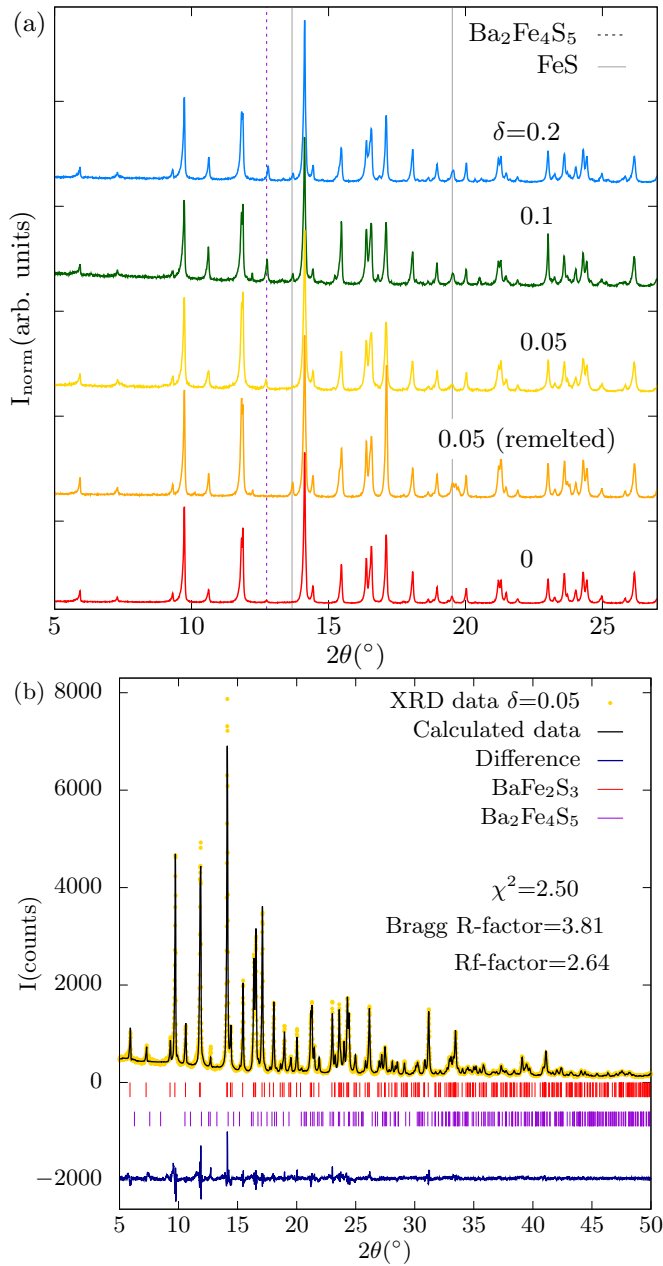


FIG. 2. (a) Powder x-ray diffraction pattern of $\text{BaFe}_{2+\delta}\text{S}_3$ for nominal $\delta = 0, 0.05, 0.1,$ and 0.2 . Vertical lines indicate the positions of the most intense reflections for the secondary phases. The patterns are vertically shifted for clarity and the intensity is normalized. (b) Rietveld analysis of the powder x-ray diffraction pattern for $\delta = 0.05$.

TABLE II. Lattice parameters as a function of the excess Fe in the nominal composition δ for $\text{BaFe}_{2+\delta}\text{S}_3$. The number in parenthesis correspond to the error of the fit.

δ	a (Å)	b (Å)	c (Å)
0	8.7759(2)	11.2177(3)	5.2823(1)
0.05 (remelted)	8.7742(4)	11.2137(5)	5.2793(2)
0.05	8.7762(3)	11.2151(4)	5.2849(2)
0.1	8.7797(4)	11.2211(5)	5.2850(2)
0.2	8.7765(3)	11.2199(4)	5.2841(2)

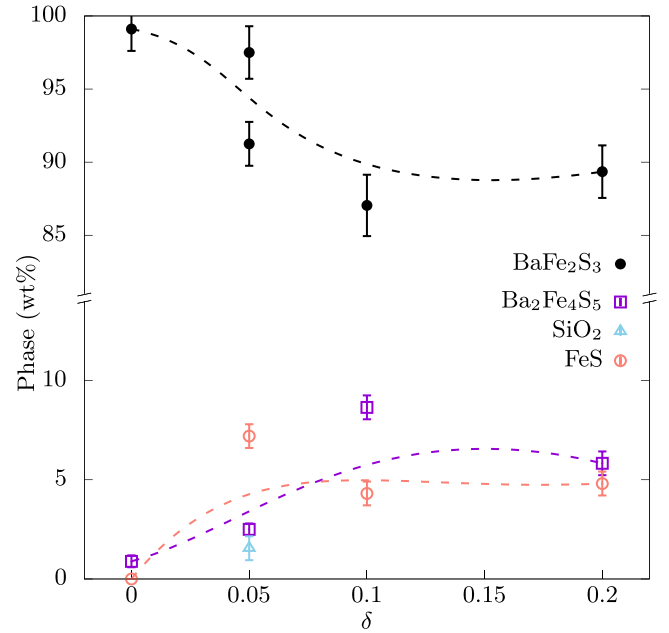


FIG. 3. Weight fraction of the phases BaFe_2S_3 , $\text{Ba}_2\text{Fe}_4\text{S}_5$, FeS , and SiO_2 as a function of the nominal Fe composition. The dotted lines are guides to the eye.

is presented in Fig. 2(b). The lattice parameters vary within 0.06–0.1%, but no systematic change can be observed as a function of δ , as presented in Table II. This is also consistent with the EDX results, which show a similar Fe stoichiometry of the main phase for all samples and no correlation with the nominal δ .

Diffraction data confirms the presence of traces (<13 wt%) of impurity phases. The extra reflections are consistent with $\text{Ba}_2\text{Fe}_4\text{S}_5$ [27] and FeS [28]. The most intense reflections of these phases are indicated with lines in Fig. 2(a). We also identify SiO_2 only for the case of $\delta = 0.05$ (remelted). The presence and nature of these inclusions are in good agreement with the EDX measurements. From the Rietveld analysis, we obtained that the fraction of overall secondary phase increases with δ , as shown in Fig. 3. The presence of a small amount of secondary phase also for $\delta = 0$ suggests incongruent melting.

2. Single crystal x-ray diffraction

Single crystal x-ray diffraction measurements were conducted to address the question of possible structural and stoichiometry variations of the main phase as a function of δ . For this purpose, single crystals with an edge length of 50 μm to 100 μm were selected. Table III summarizes parameters of the data collection and the results of the structural refinement. The atomic positions, isotropic and anisotropic displacement parameters are listed in Tables IV and V. No clear monotonic variation of atomic positions, isotropic nor anisotropic displacement parameters is observed.

In line with former studies [4,16] and with the results of the powder x-ray diffraction, the analysis of systematic extinctions and the subsequent structure refinements confirm that BaFe_2S_3 crystallizes in the orthorhombic space group $Cmcm$ (No. 63). Since BaFe_2S_3 was suggested to be prone to Fe deficiency and a considerable amount of Fe vacancies

TABLE III. Details on data collection and structure refinement of BaFe_{2+δ}S₃ as determined from single-crystal x-ray diffraction as a function of the nominal Fe content δ. The lattice parameters were obtained from the Rietveld refinement of the powder x-ray diffraction data.

nominal δ	0	0.05 (remelted)	0.05	0.1	0.2
Crystal data					
Temperature (K)	295	295	295	295	295
Space group	<i>Cmcm</i>	<i>Cmcm</i>	<i>Cmcm</i>	<i>Cmcm</i>	<i>Cmcm</i>
<i>a</i> (Å)	8.7759(2)	8.7742(4)	8.7762(3)	8.7797(4)	8.7765(3)
<i>b</i> (Å)	11.2177(3)	11.2137(5)	11.2151(4)	11.2211(5)	11.2199(4)
<i>c</i> (Å)	5.2823(1)	5.2793(2)	5.2849(2)	5.2850(2)	5.2841(2)
<i>Z</i>	4	4	4	4	4
<i>M_r</i>	345.17	345.17	345.17	345.17	345.17
ρ _{calc} (g cm ⁻³)	4.408	4.412	4.408	4.406	4.407
μ (mm ⁻¹)	14.014	14.026	14.016	14.010	14.011
Data collection					
2 θ _{max} (°)	62.938	62.968	62.932	62.922	54.95
Absorption correction	Multiscan	Multiscan	Multiscan	Multiscan	Multiscan
T _{min}	0.5527	0.6714	0.6105	0.4501	0.4644
T _{max}	0.7462	0.7462	0.7462	0.7462	0.7462
N _{measured}	5269	6017	4441	4482	2295
N _{independent}	486	486	489	505	354
R _{int} (%)	2.97	3.56	1.99	2.16	2.5
Refinement					
N _{parameters}	20	20	20	20	20
R ₁ > 4σ (%)	1.69	1.48	1.11	1.14	1.27
R ₁ all (%)	2.33	2.07	1.36	1.28	1.44
wR ₂ > 4σ (%)	3.12	2.83	2.29	2.52	2.60
wR ₂ all (%)	3.27	2.98	2.34	2.56	2.65
G.O.F	1.137	1.091	1.055	1.105	1.086
Δρ _{min} (e Å ⁻³)	-0.756	-0.797	-0.371	-0.670	-0.372
Δρ _{max} (e Å ⁻³)	0.949	0.942	0.719	1.001	1.002
weight <i>w</i> (<i>a, b</i>)	0.0138	0.0136	0.0108	0.0094	0.0114
	1.0487	0.4001	0.5927	0.9146	0.2287

T_{min} = minimum transmission, T_{max} = maximum transmission, $R_1 = \sum \|F_0\| - \|F_c\| / \sum \|F_0\|$, $wR_2 = \{\sum [w(F_0^2 - F_c^2)^2] / \sum [w(F_0^2)^2]\}^{1/2}$, $w = 1/[(\sigma^2(F_0^2)) + (aP)^2 + bP]$ where $P = [2F_c^2 + \max(F_0^2, 0)]/3$

TABLE IV. Atomic coordinates and equivalent isotropic displacement parameters of BaFe_{2+δ}S₃ single crystals at 295 K as a function of the nominal Fe content δ.

nominal δ	0	0.05 (remelted)	0.05	0.1	0.2
Ba					
<i>x</i>	0.5	0.5	0.5	0.5	0.5
<i>y</i>	0.18616(3)	0.18623(3)	0.18631(2)	0.18633(2)	0.18634(3)
<i>z</i>	0.25	0.25	0.25	0.25	0.25
U _{eq} (Å ²)	0.01878(8)	0.01893(8)	0.01819(6)	0.01881(6)	0.01842(9)
Fe					
<i>x</i>	0.34631(5)	0.34636(4)	0.34628(3)	0.34630(3)	0.34629(4)
<i>y</i>	0.5	0.5	0.5	0.5	0.5
<i>z</i>	0	0	0	0	0
U _{eq} (Å ²)	0.01119(10)	0.01155(9)	0.01086(7)	0.01148(7)	0.01122(11)
S ₁					
<i>x</i>	0.5	0.5	0.5	0.5	0.5
<i>y</i>	0.61574(9)	0.61580(8)	0.61576(6)	0.61575(6)	0.61553(9)
<i>z</i>	0.25	0.25	0.25	0.25	0.25
U _{eq} (Å ²)	0.01135(20)	0.01156(19)	0.01114(13)	0.01170(12)	0.01151(20)
S ₂					
<i>x</i>	0.20756(11)	0.20748(8)	0.20749(6)	0.20757(7)	0.20746(9)
<i>y</i>	0.37843(8)	0.37830(7)	0.37831(5)	0.37825(6)	0.37836(8)
<i>z</i>	0.25	0.25	0.25	0.25	0.25
U _{eq} (Å ²)	0.01946(18)	0.01950(16)	0.01883(11)	0.01940(11)	0.01937(18)

TABLE V. Anisotropic displacement parameters of $\text{BaFe}_{2+\delta}\text{S}_3$ single crystals at 295 K as a function of the nominal Fe content δ .

nominal δ	0	0.05 (remelted)	0.05	0.1	0.2
Ba					
U_{11} (\AA^2)	0.02021(17)	0.01964(12)	0.01934(9)	0.01975(9)	0.01835(15)
U_{22} (\AA^2)	0.02223(14)	0.02206(13)	0.02123(9)	0.02109(9)	0.02160(16)
U_{33} (\AA^2)	0.01390(11)	0.01508(15)	0.01401(10)	0.01560(9)	0.01529(13)
Fe					
U_{11} (\AA^2)	0.01072(24)	0.01028(16)	0.01046(12)	0.01081(13)	0.00958(21)
U_{22} (\AA^2)	0.01465(20)	0.01509(18)	0.01433(12)	0.01409(13)	0.01511(24)
U_{33} (\AA^2)	0.00821(17)	0.00929(22)	0.00779(14)	0.00953(13)	0.00899(17)
U_{23} (\AA^2)	0.00004(14)	0.00030(15)	0.00006(10)	0.00016(10)	0.00003(14)
S₁					
U_{11} (\AA^2)	0.01295(56)	0.01197(37)	0.01196(27)	0.01245(28)	0.01076(46)
U_{22} (\AA^2)	0.01101(44)	0.01177(40)	0.01154(26)	0.01146(27)	0.01248(52)
U_{33} (\AA^2)	0.01010(38)	0.01096(51)	0.00992(33)	0.01118(29)	0.01128(40)
S₂					
U_{11} (\AA^2)	0.01994(47)	0.01908(31)	0.01897(23)	0.01960(24)	0.01831(38)
U_{22} (\AA^2)	0.02679(41)	0.02655(37)	0.02577(25)	0.02560(26)	0.02657(45)
U_{33} (\AA^2)	0.01165(29)	0.01388(41)	0.01175(25)	0.01301(23)	0.01322(30)
U_{12} (\AA^2)	-0.01233(37)	-0.01230(30)	-0.01198(21)	-0.01212(22)	-0.01256(18)

was claimed for $\delta < 0.1$ [16], we refined the Fe occupancy of our single crystals. No significant deviation from the ideal stoichiometry could be detected for our samples; i.e., irrespective of the nominal δ value, we found $\text{BaFe}_{2+\delta}\text{S}_3$ with $\delta = 0$. Furthermore, keeping the site occupancy variable for the remaining atoms did not show a statistically relevant off-stoichiometry. Similar to the closely related Se compound, BaFe_2Se_3 , the maximum residual electron density was observed in the vicinity of the Ba atom. This residual electron density was interpreted earlier as a result of the motion of the weakly bonded Ba atom [29]. This is perfectly in-line with the EDX results described above.

Figure 4 shows the crystal structure of BaFe_2S_3 based on our refinement. The c axis was found to be parallel to the long direction of the needle-like crystals. The main structural units are two-leg Fe-ladders, assembled by edge-sharing FeS_4 tetrahedra, running along the crystallographic c direction and channels occupied by Ba atoms. The two Fe-Fe distances in the ladder are $d_{\text{rung}} = 2.6976(9)$ \AA (parallel to a) and $d_{\text{leg}} = 2.64115(5)$ \AA (parallel to c) for $\delta = 0$. These values scatter within 0.1% as a function of δ . The strong anisotropy of the atomic displacement parameters (ADP) for the S_2 site, see Table V, is in agreement with the findings by Hong and Steinfink [4]. The long axis of the elongated “cigar-shaped” ADP ellipsoid lies in the ab plane and is almost perpendicular to the Fe- S_2 bond. This may indicate the tendency to break the symmetry by a rotation of the FeS_4 tetrahedra within the ab plane similar to the temperature-dependent $Cmcm$ to $Pnma$ phase transition in BaFe_2S_3 [30].

C. Magnetization

Figure 5(a) presents the magnetization divided by the applied magnetic field M/H as a function of the temperature T for different nominal Fe compositions and a magnetic field of $\mu_0 H = 5$ T parallel to the c axis. We used such a high magnetic field in order to try to saturate any possible ferromagnetic spurious contribution (see below). Below

room temperature, the magnetization decreases with decreasing temperature. This tendency, that contrasts the typical Curie-Weiss behavior observed in 3D localized magnets, is independent of δ and is also commonly observed in other quasi-1D materials [31,32]. This behavior can be qualitatively understood if we consider that low-dimensional magnets show short range correlations at temperatures above T_N , which will be reflected in a maximum in the susceptibility at a temperature of the order of these correlations. For temperatures below the maximum, one observes a decreasing susceptibility for

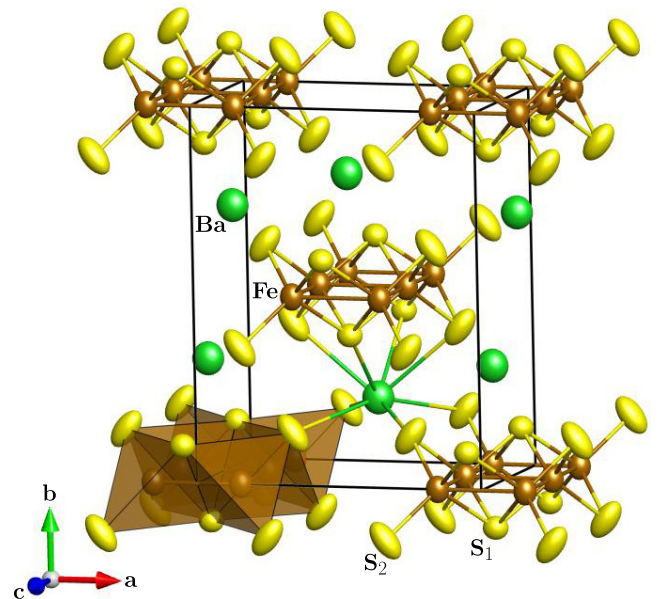


FIG. 4. Crystal structure of orthorhombic BaFe_2S_3 obtained for $\delta = 0$ from single crystal x-ray diffraction measurements. Samples with other δ values exhibit a very similar structure, see Tables III, IV, and V.

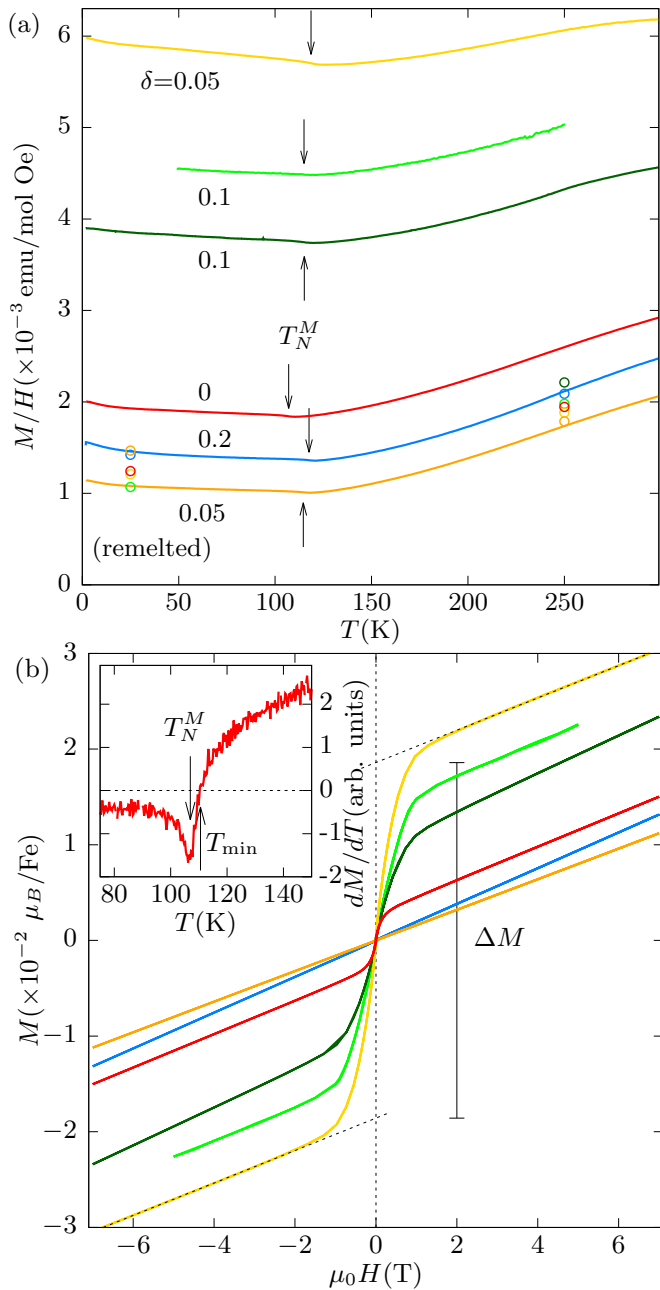


FIG. 5. (a) Magnetization of $\text{BaFe}_{2+\delta}\text{S}_3$ as a function of temperature for crystals with different nominal Fe content. The arrows indicate the Néel temperature as defined in the inset. The circles are the susceptibility obtained from $M(H)$ for fields above 4 T. The color indicates the value of δ . Measurements for two samples of the same batch are shown for $\delta = 0.1$. (b) Field dependence of the magnetization for the same samples of (a) for $T = 250$ K. ΔM indicates the contribution of extrinsic magnetic inclusions for $\delta = 0.05$. Inset: Definitions of the characteristic temperatures for the case of $\delta = 0$.

decreasing temperature. The change of behavior at around ~ 120 K marks the antiferromagnetic transition. Below T_N , the direction of the applied magnetic field is perpendicular to the magnetic moments as presented in Ref. [1].

It is noticeable that δ affects the absolute value of $M/H(T)$ in a nonmonotonous way, as can be observed in Fig. 5(a).

This is also reflected in the jump at low fields (ΔM) in the isothermal magnetization for $T = 250$ K shown in Fig. 5(b). A similar jump is also found in measurements below T_N (not shown). This kind of behavior was already reported in the literature [33] and was also associated with an extrinsic ferromagnetic contribution. We find that the size of ΔM depends in an arbitrary manner on the particular sample, as shown for $\delta = 0.1$ in Figs. 5(a) and 5(b). This is consistent with the presence of extrinsic ferromagnetic inclusions in different amounts in different samples even of the same batch. If we assume that the magnetic inclusion is Fe, it represents less than 2 mol% for all samples. Such a small fraction of Fe most likely remains undetected in powder x-ray diffraction measurements, but is occasionally seen in EDX analysis, see Fig. 1(d). It is worth to mention that remelted samples ($\delta = 0.05$) have $\Delta M \simeq 0$, which indicates that practically no spurious ferromagnetic phase is present.

In order to get rid of the extrinsic ferromagnetic contribution, the magnetic susceptibility can be calculated from the slope of $M(H)$ well above the characteristic field of the magnetization jump (Honda-Owen analysis, see Ref. [34]), where the spurious contribution is essentially saturated. While M/H varies by a factor of six between samples, the susceptibility (dM/dH) varies by less than 50%, see Fig. 5(a). The obtained dM/dH values (1.07 – 1.47×10^{-3} emu/mol Oe for 25 K) are close to $M/H(T)$ of the remelted sample. Therefore, remelted samples may be assumed to show the behavior closest to the intrinsic one of BaFe_2S_3 .

However, the value of the susceptibility obtained from the high-field slope of $M(H)$ still presents a small sample dependence that it is neither correlated with the presence of ferromagnetic impurities nor to δ . Further, this variations are too large to be originated in crystal misalignment, especially in the paramagnetic phase [1]. Since we know from EDX and powder x-ray diffraction that other magnetic impurity phases may be present (such as antiferromagnetic FeS [35]), these variations in dM/dH do not necessarily correspond to variations in the main phase. Further insight can be gained by analyzing the behavior of the Néel temperature.

We define the Néel temperature (T_N^M) as the minimum of the temperature derivative of the magnetization ($\frac{dM}{dT}|_{\min}$). Notice that some authors use the temperature at which the magnetization has a minimum (T_{\min}) to estimate the transition temperature [16,33]. Although both quantities do not result in the same numerical value, see inset of Fig. 5(b), they are expected to be closely correlated if they are both meaningful indicators of the magnetic phase transition of the main phase. Figure 6 shows that this is not the case. Both quantities are not equivalent, while there is an appreciable dispersion in T_{\min} for different samples, even of the same batch, T_N^M is less sensitive to sample variations within a batch. The samples with the least amount of ferromagnetic impurity exhibit the smallest difference between both quantities and this difference is largest for samples with higher values of T_{\min} , see inset of Fig. 6. This suggests that the value of T_{\min} is more susceptible to the ferromagnetic impurities than T_N^M and that a high value of T_{\min} does not necessarily correspond to a higher chemical purity of the sample, in contrast to what is commonly assumed. Irrespective of the quantity chosen, there is no clear dependence on δ , but different values of T_N are

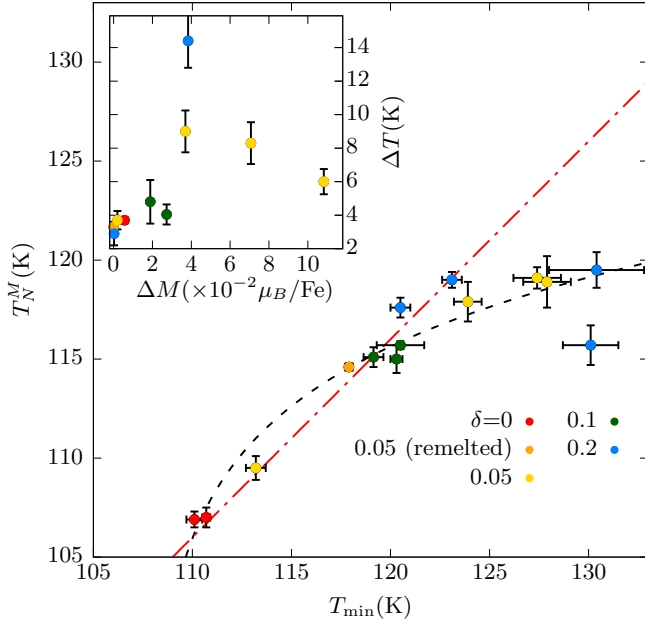


FIG. 6. Correlation between T_{\min} and T_N^M . The different data points for the same value of δ correspond to measurements of different samples of the same batch, with the exception for the case of $\delta = 0.05$ where data from two different batches are presented in yellow. The dotted lines are guides to the eye to indicate a linear and nonlinear dependence. Inset: $T_{\min} - T_N^M$ as a function of ΔM for $T = 250$ K.

observed for different samples within a batch. Samples with $\delta = 0$ appear to present a consistently lower value for T_N , but such low T_N values are observed in samples with $\delta = 0.05$ as well. However, the structural and compositional analysis of the $\delta = 0$ batch is in no way conspicuous. The differences in T_N might be related to a small amount of disorder.

D. Resistivity

Figure 7(a) presents the resistivity as a function of the inverse temperature for samples with different nominal Fe composition. The resistivity increases with decreasing temperature indicating an insulating behavior. This behavior is shared by all samples in spite of the different nominal δ value. Two characteristic temperatures can be identified, the Néel temperature at $T_N^\rho \sim 120$ K and a slope change at $T^* \sim 190$ K, as indicated in Fig. 7(a). The definition used for these characteristic temperatures is shown in Fig. 7(b): T_N^ρ is marked by the presence of a maximum, while T^* corresponds to a minimum in $d\ln\rho/d(1/T)$. The origin of the change at T^* is still under debate, but it has been suggested to be related to an orbital ordering transition [3,16]. The samples with $\delta = 0$ present the lowest value of T_N^ρ , as already observed in magnetization measurements, and a visibly larger broadening of the logarithmic derivative in the area around T_N^ρ , as shown in Fig. 7(b).

For $\delta \geq 0.05$ and $T \lesssim 90$ K, $d\ln\rho/d(1/T)$ is practically temperature independent, which allows us to describe the resistivity with a thermally activated behavior ($\rho = \rho_0 e^{\Delta/T}$), as shown in Fig. 7(b). The same kind of behavior is also observed by Hirata *et al.* [16] but only for $\delta = 0.1$. The resulting gap

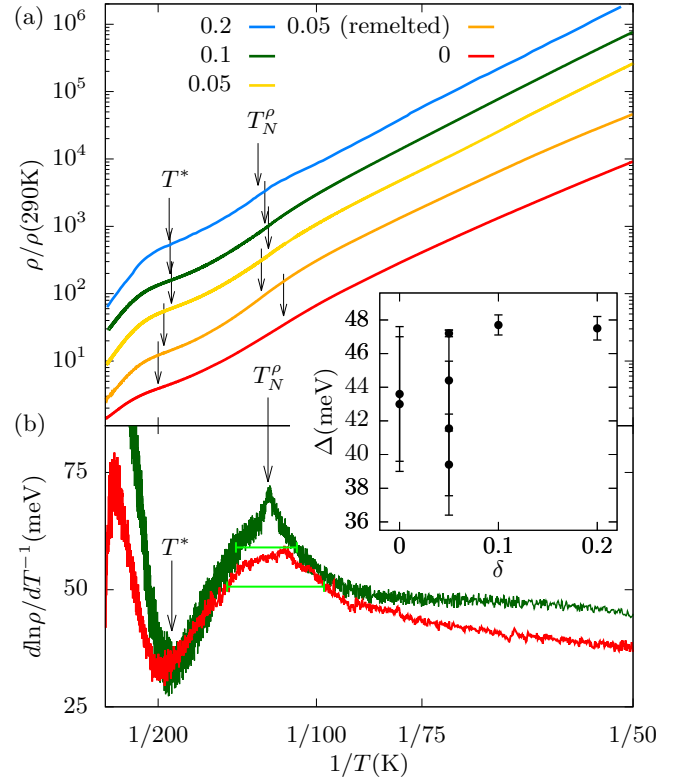


FIG. 7. (a) Normalized resistivity as a function of the inverse temperature for different nominal values of δ for $\text{BaFe}_{2+\delta}\text{S}_3$. The curves are vertically shifted for clarity. (b) Temperature dependence of the derivative of the logarithmic of the resistivity with respect to the inverse temperature for $\delta = 0.1$ and 0. T_N^ρ and T^* are indicated with an arrow for $\delta = 0.1$. The horizontal segments indicate the broadening of the curves around T_N^ρ , computed as the width of the curves at half of the distance from their maximum to the value of Δ . Inset: Value of the energy gap for $T < T_N^\rho$ as a function of the nominal Fe content.

(Δ) from our data for different δ values is plotted in the inset of Fig. 7, and is in a good agreement with the value for $\delta = 0.1$ from the literature (47 meV) [16]. For $\delta \leq 0.05$, the resistivity slightly deviates from a thermally activated behavior. For completeness, the obtained gap in these cases using as fitting interval the range 60 K to 90 K is also included in the inset of Fig. 7. A 1D-variable range hopping, $\rho = \rho_0 e^{(T_0/T)^{1/2}}$ [36], is found to quantitatively fit the resistivity below ~ 90 K for $\delta = 0$. This kind of behavior has been previously observed in the literature [16,33].

IV. DISCUSSION

Figure 8(a) summarizes the Néel temperature and T^* obtained for samples with different nominal Fe content. T^* is present for all samples independent of the value of δ and has a variation of less than 8%. T_N as estimated from resistivity measurements (as defined in Fig. 7) and from the magnetization [inset Fig. 5(b)] presents only a weak increase with δ . This contrasts with Ref. [16], where a change in T_N of ~ 40 K was reported across $0 \leq \delta \leq 0.2$ with a maximum for $\delta = 0.1$. However, this maximum is only apparent, since only T_N for a single sample is presented at each δ in Ref. [16]. We

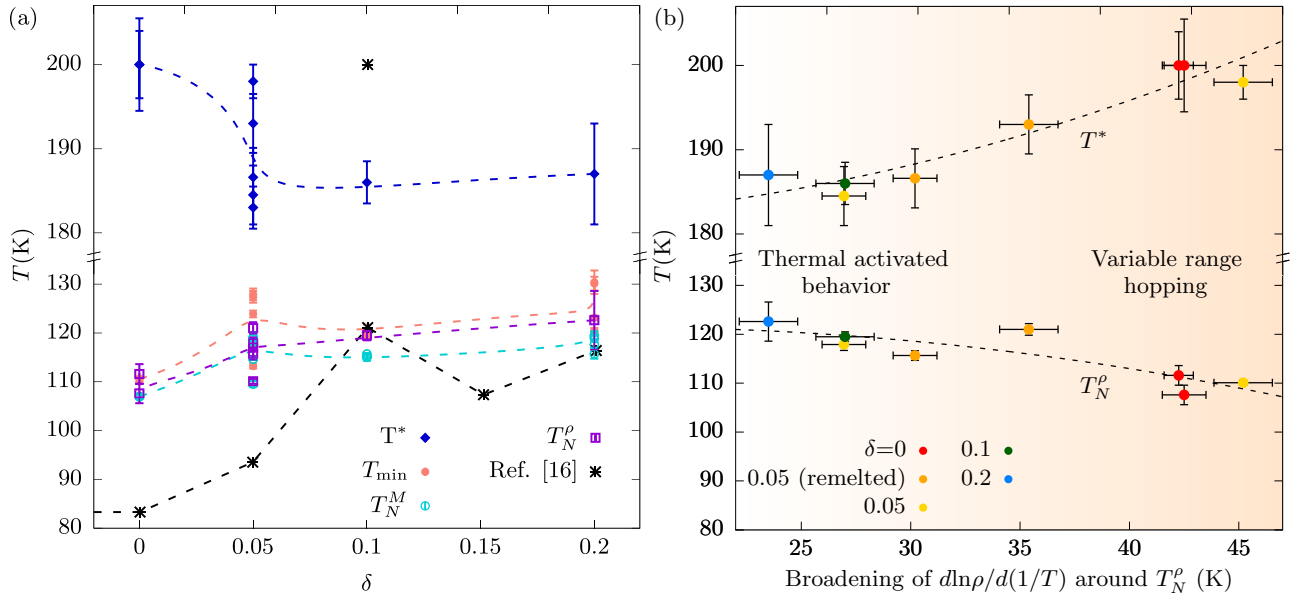


FIG. 8. (a) Dependence of T_N^ρ and T^* with the nominal Fe content for $\text{BaFe}_{2+\delta}\text{S}_3$. T_{\min} , T_N^M , and T_N^ρ correspond to the Néel temperature obtained from magnetization [inset of Fig. 5(b)] and resistivity measurements (Fig. 7), respectively. For each value of δ , data from several samples are presented. For comparison, T_N and T^* extracted from reference [16] are also included. The dotted lines are guides to the eye. (b) T_N^ρ and T^* as a function of the broadening of $d \ln \rho / d(1/T)$ around T_N^ρ as defined in Fig. 7(b). The dotted lines are guides to the eye. The background color indicates the change from thermal activated behavior to variable range hopping. Samples from two batches are presented for the case of $\delta = 0.05$ in addition to the remelted samples.

show that similar and higher values of T_N are also observed in some samples with $\delta = 0.05$ and 0.2 . This is consistent with the fact that no systematic shift in the average composition or structure was observed as a function of δ and suggests a relatively small amount of disorder as the source of the variations in T_N .

For metallic samples, the residual resistivity is often used as an indicator of disorder that may remain undetected in other methods. A clear correlation between the residual resistivity and the critical temperature for superconductivity has been reported for several systems [37,38]. However, as shown in Fig. 7(a), the insulating character of the resistivity of BaFe_2S_3 crystals rules out using the residual resistivity value as an estimator for the level of disorder. On the other hand, the logarithmic derivative of the resistivity shows a broad maximum at $\sim T_N$. The width of this peak varies for each sample, and is correlated with the value of T_N and T^* , as shown in Fig. 8(b): The peak is narrower when T_N is higher and T^* is lower. In addition, for samples where the peak is narrower, the resistivity below 100 K follows more closely a thermally activated behavior [$d \ln \rho / d(1/T)$ is closer to a constant]. This suggests that the peak width may be an indicator of disorder in the sample, analogous to the residual resistivity in metals.

The inhomogeneity of T_N and T^* observed within a batch is most probably related to the method used to obtain the crystals. Adding excess Fe acts as a “self-flux”, and as the crystallization progresses, the composition of the liquid continuously changes. Therefore, crystals forming from the liquid at different points in time at different temperature can exhibit slightly different composition or level of impurities (e.g., coming from the crucible or the limited purity of the chemical precursors). Although this problem is not avoided by using the

Bridgman method, the high temperature gradient provides for better conditions for crystallization and leads to a suppression of ferromagnetic impurities in the crystal.

A further improvement in this sense would be the growth of BaFe_2S_3 crystals using the floating-zone method, which not only offers higher temperature gradients on the crystallization front, but is also crucible free. The ubiquitous presence of secondary phases is possibly indicative of incongruent melting of BaFe_2S_3 : the floating zone technique provides, once the molten zone is stabilized, a “self-adjusted flux” that favors crystal homogeneity.

V. CONCLUSIONS

We have studied the effect of the nominal Fe excess in $\text{BaFe}_{2+\delta}\text{S}_3$ in the composition, the crystal structure, the magnetization, and the resistivity. The analysis of the composition, as well as the crystal structure, obtained from powder and single crystal x-ray diffraction measurements, indicate that the extra Fe induces the formation of Fe-rich inclusions rather than being incorporated in the structure. The nature of these extra phases depends on the value of δ and they are not homogeneously distributed within a batch. Magnetic inclusions affect the experimentally observed magnetization curves, giving rise to higher absolute values of M/H and a magnetization step in $M(H)$. Moreover, we found that ferromagnetic inclusions, ubiquitous to samples grown as indicated in the literature, can be excluded by directional crystallization of remelted samples using Bridgman-like process based on optical heating, thereby allowing the study of the intrinsic properties of BaFe_2S_3 . The magnetization and the resistivity are consistent with an antiferromagnetic transition

at $T_N \sim 120$ K and, in contrast with a previous work [16], we observed a small variation in T_N as a function of δ that strongly contrasts the maximum reported for $\delta = 0.1$. Moreover, we presented a correlation between T_N and T^* with the broadening of the logarithmic derivative of the resistivity around $\sim T_N$ that could be an indicator of the level of disorder in the samples. This inhomogeneity in the samples is characteristic of the “flux”-like growth procedure and could be considerable improved by using the floating-zone technique.

Note added in proof. Recently, single crystals of BaFe_2S_3 were successfully grown with a laser-assisted floating zone technique resulting in large samples free of ferromagnetic impurities [39].

ACKNOWLEDGMENTS

We thank G. Kreutzer and S. Müller-Litvanyi for the assistance in the EDX measurements, C.G.F. Blum for the assistance in the powder x-ray measurements, S. Gaß and G. Bastien for technical assistance in the magnetization measurements and F. Cagliaris and C. Wuttke for technical assistance in the resistivity measurements. This research has been supported by the Deutsche Forschungsgemeinschaft (DFG) through SFB 1143 (Project No. 247310070), the DFG within the Graduate School GRK 1621 and the Würzburg-Dresden Cluster of Excellence on Complexity and Topology in Quantum Matter - ct.qmat (EXC 2147, Project No. 390858490). M.L.A. acknowledges support from the Alexander von Humboldt Foundation through the Georg Forster program.

-
- [1] H. Takahashi, A. Sugimoto, Y. Nambu, T. Yamauchi, Y. Hirata, T. Kawakami, M. Avdeev, K. Matsubayashi, F. Du, C. Kawashima *et al.*, *Nat. Mater.* **14**, 1008 (2015).
- [2] J. Ying, H. Lei, C. Petrovic, Y. Xiao, and V. V. Struzhkin, *Phys. Rev. B* **95**, 241109(R) (2017).
- [3] T. Yamauchi, Y. Hirata, Y. Ueda, and K. Ohgushi, *Phys. Rev. Lett.* **115**, 246402 (2015).
- [4] H. Hong and H. Steinfink, *J. Solid State Chem.* **5**, 93 (1972).
- [5] E. Dagotto and T. Rice, *Science* **271**, 618 (1996).
- [6] K. Magishi, S. Matsumoto, Y. Kitaoka, K. Ishida, K. Asayama, M. Uehara, T. Nagata, and J. Akimitsu, *Phys. Rev. B* **57**, 11533 (1998).
- [7] L. Craco and S. Leoni, *Phys. Rev. B* **98**, 195107 (2018).
- [8] S. Roh, S. Shin, J. Jang, S. Lee, M. Lee, Y.-S. Seo, W. Li, T. Biesner, M. Dressel, J. Y. Rhee, T. Park, and J. Hwang, *Phys. Rev. B* **101**, 115118 (2020).
- [9] J. M. Pizarro and E. Bascones, *Phys. Rev. Mater.* **3**, 014801 (2019).
- [10] Y. Zhang, L. Lin, J.-J. Zhang, E. Dagotto, and S. Dong, *Phys. Rev. B* **95**, 115154 (2017).
- [11] P. Materne, W. Bi, J. Zhao, M. Y. Hu, M. L. Amigó, S. Seiro, S. Aswartham, B. Büchner, and E. E. Alp, *Phys. Rev. B* **99**, 020505(R) (2019).
- [12] L. Zheng, B. A. Frandsen, C. Wu, M. Yi, S. Wu, Q. Huang, E. Bourret-Courchesne, G. Simutis, R. Khasanov, D.-X. Yao, M. Wang, and R. J. Birgeneau, *Phys. Rev. B* **98**, 180402(R) (2018).
- [13] M. S. Torikachvili, S. L. Bud'ko, N. Ni, and P. C. Canfield, *Phys. Rev. Lett.* **101**, 057006 (2008).
- [14] H. Okada, K. Igawa, H. Takahashi, Y. Kamihara, M. Hirano, H. Hosono, K. Matsubayashi, and Y. Uwatoko, *J. Phys. Soc. Jpn.* **77**, 113712 (2008).
- [15] H. Sun, X. Li, Y. Zhou, J. Yu, B. A. Frandsen, S. Wu, Z. Xu, S. Jiang, Q. Huang, E. Bourret-Courchesne, L. Sun, J. W. Lynn, R. J. Birgeneau, and M. Wang, *Phys. Rev. B* **101**, 205129 (2020).
- [16] Y. Hirata, S. Maki, J.-i. Yamaura, T. Yamauchi, and K. Ohgushi, *Phys. Rev. B* **92**, 205109 (2015).
- [17] C. Stinn, K. Nose, T. Okabe, and A. Allanore, *Metall. Mater. Trans. B* **48**, 2922 (2017).
- [18] M. Neubronner, T. Bodmer, C. Hübner, P. B. Kempa, E. Tsotsas, A. Eschner, G. Kasperek, F. Ochs, H. Müller-Steinhagen, H. Werner, and M. H. Spitzner, D6 properties of solids and solid materials: Datasheet from VDI-Buch.
- [19] S. Seiro, M. Deppe, H. Jeevan, U. Burkhardt, and C. Geibel, *Phys. Status Solidi B* **247**, 614 (2010).
- [20] J. Rodríguez-Carvajal, *Phys. B: Condens. Matter* **192**, 55 (1993).
- [21] Bruker, APEX3 v2018.1-0, Bruker AXS Inc., Madison, Wisconsin, USA (2017).
- [22] SAINT(V8.30A), Bruker AXS Inc., Madison, Wisconsin, USA (2017).
- [23] L. Krause, R. Herbst-Irmer, G. M. Sheldrick, and D. Stalke, *J. Appl. Crystallogr.* **48**, 3 (2015).
- [24] G. M. Sheldrick, *Acta Crystallogr. Sect. A* **64**, 112 (2008).
- [25] L. J. Farrugia, *J. Appl. Crystallogr.* **32**, 837 (1999).
- [26] J. Goldstein, D. E. Newbury, D. C. Joy, C. E. Lyman, P. Echlin, E. Lifshin, L. Sawyer, and J. R. Michael, *Scanning Electron Microscopy and X-ray Microanalysis* (Springer, New York, 2003).
- [27] J. S. Swinnea, G. Eisman, T. Perng, N. Kimizuka, and H. Steinfink, *J. Solid State Chem.* **41**, 104 (1982).
- [28] W. G. Marshall, R. J. Nelmes, J. S. Loveday, S. Klotz, J. M. Besson, G. Hamel, and J. B. Parise, *Phys. Rev. B* **61**, 11201 (2000).
- [29] B. Saparov, S. Calder, B. Sipoš, H. Cao, S. Chi, D. J. Singh, A. D. Christianson, M. D. Lumsden, and A. S. Sefat, *Phys. Rev. B* **84**, 245132 (2011).
- [30] V. Svitlyk, D. Chernyshov, E. Pomjakushina, A. Krzton-Maziopa, K. Conder, V. Pomjakushin, R. Pöttgen, and V. Dmitriev, *J. Phys.: Condens. Matter* **25**, 315403 (2013).
- [31] D. C. Johnston, *Phys. Rev. B* **54**, 13009 (1996).
- [32] S. K. Tiwary and S. Vasudevan, *Solid State Commun.* **101**, 449 (1997).
- [33] X. Zhang, H. Zhang, Y. Ma, L. Wang, J. Chu, T. Hu, G. Mu, Y. Lu, C. Cai, F. Huang *et al.*, *Sci. China: Phys., Mech. Astron.* **61**, 077421 (2018).
- [34] L. F. Bates, *Modern Magnetism* (Cambridge University Press, Cambridge, 1948).
- [35] E. Hirahara and M. Murakami, *J. Phys. Chem. Solids* **7**, 281 (1958).

- [36] M. M. Fogler, S. Teber, and B. I. Shklovskii, *Phys. Rev. B* **69**, 035413 (2004).
- [37] A. P. Mackenzie, R. K. W. Haselwimmer, A. W. Tyler, G. G. Lonzarich, Y. Mori, S. Nishizaki, and Y. Maeno, *Phys. Rev. Lett.* **80**, 161 (1998).
- [38] H. Hobou, S. Ishida, K. Fujita, M. Ishikado, K. M. Kojima, H. Eisaki, and S. Uchida, *Phys. Rev. B* **79**, 064507 (2009).
- [39] M. L. Amigó, A. Maljuk, K. Manna, Q. Stahl, C. Felser, C. Hess, A. U. B. Wolter, J. Geck, S. Seiro, and B. Büchner, *Crystals* **11**, 758 (2021).